Journal of Solid State Chemistry **157,** 30–39 (2001)
doi:10.1006/jssc.2000.9033, available online at http://www.idealibrary.com on IDEAL®

Decomposition of MgF_2 in the Transmission Electron Microscope

Lars-Peter Zenser[1] and Reginald Gruehn[2]

Institut für anorganische und analytische Chemie II, Justus-Liebig-Universität, Heinrich-Buff-Ring 58, D–35392 Giessen, Germany

and

Bernd H. Liebscher

Institut für Mineralogie, Goethe-Universität, Senkenberganlage 28, D–60054 Frankfurt/Main, Germany

Received June 29, 2000; in revised form October 27, 2000; accepted December 1, 2000

The decomposition of thin MgF_2 crystals, crystallized by chemical vapor transport, can be observed in brightfield mode in the transmission electron microscope. EELS and diffraction studies showed that the decomposition process leads via metallic magnesium to MgO. Single crystals from MgF_2 were obtained by chemical vapor transport using iodine as transport agent.

Key Words: **decomposition; EELS; diffraction; MgF_2; TEM.**

1. INTRODUCTION

In analytical electron microscopy (AEM) radiation damage is an often observed problem. Since the beginning of AEM it was subject to explanations and research (see Howitt (12) and Hren (13)).

Damage to biological materials and organic substances is nearly impossible to avoid, but it can also be observed on inorganic materials. For example, carbonates decompose under an electron probe (1), like zeolites (30); under heavy radiation crystalline quartz changes its appearance to amorphous silica (4). Even oxides can be destroyed by intensive electron radiation (26).

Compared to other inorganic compounds, the alkali halides form quite beam-sensitive specimens (12, 15). The behavior of alkali earth fluorides in the transmission electron microscope (TEM) was investigated in recent work (CaF_2, (7, 15, 19); SrF_2, (7)). Evans (7) evaluated the observed Moiré patterns of the intermediates to get information about the decomposition of calcium fluoride and strontium fluoride on the crystallographical lattice. The irradiation damage process caused by the electron probe proceeds similarly in CaF_2 and SrF_2. In both cases the formation of metallic calcium and strontium was the result of the decomposition. After further irradiation the Moiré patterns became diffuse and disappeared; the explanation for this fact was still a problem (7).

Chemical transport reactions (9, 24) give well-shaped crystals unexpectedly from MgF_2 with iodine as transport agent (31). MgF_2 crystals (synthetic sellaite) were examined in the TEM as lighter homologues of CaF_2 and SrF_2 but with a different structure to learn something about their behavior in an electron beam.

In preliminary measurements we found that MgF_2 is decomposed, like the heavier homologues of the alkali earth fluorides CaF_2 and SrF_2. Irradiation by electrons leads to destruction of the structure. The MgF_2 crystals appeared like a single crystal before the beam was centered and focused on the specimen, as usual for EELS measurements. After that the area where the beam illuminated the specimen seemed inhomogeneous, but it showed small crystallites without a uniform orientation (Fig. 1).

Obviously there was a destruction of the crystal lattice. The main objective for our research was to determine if there is a chemical change parallel to the lattice change.

Using EELS, EDX, and electron diffraction the decomposition process of MgF_2 in TEM was analyzed from the beginning via the intermediate to the product and will be presented in this paper.

2. EXPERIMENTAL DETAILS

2.1. Preparation of MgF_2

Powdered MgF_2 was dried in a silica tube which was closed on one side at 750°C under a dynamic vacuum

[1] Part of Lars-Peter Zenser's dissertation (31).

[2] To whom correspondence should be addressed. E-mail: reginald.gruehn@anorg.chemie.uni-giessen.de.

0022-4596/01 $35.00

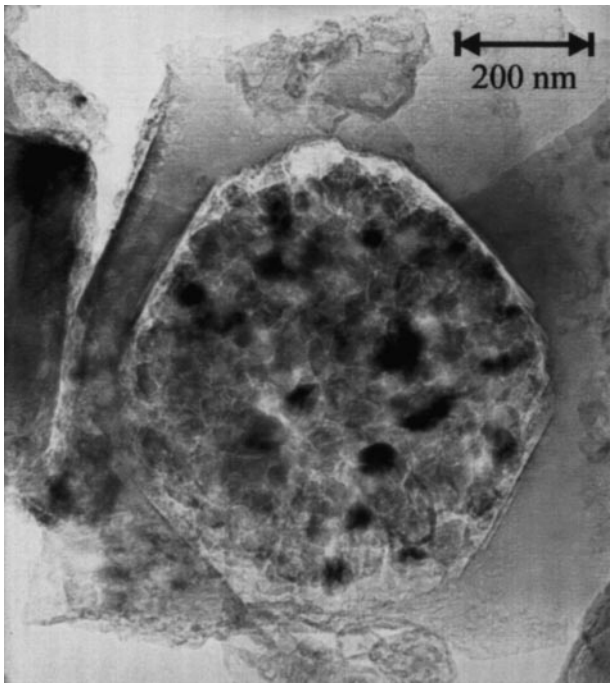

FIG. 1. Brightfield image of a crystal of MgF_2 (see scale in figure) after an exposure typical for EELS conditions.

TABLE 1
Experimental Conditions during EELS Analysis in TEM (This Work)

Acceleration potential	300 kV
TEM mode	Diffraction (camera length 300 mm)
PEELS entrance aperture	2 mm
Convergence angle α	1.2 mrad
Acceptance angle β	8.3 mrad
Energy dispersion	0.5 eV or 1.0 eV
FWHM[a]	0.9 eV to 1.4 eV

[a] Full width at half-maximum.

($\approx 7.5 \times 10^{-5}$ Pa) for about 4 hours. After addition of the transport agent (iodine, SiI_4 respectively) the ampoule was closed and heated in a temperature gradient ($\Delta T = 100°C$), usually 1000°C (source) → 900°C (sink). After 7 or 8 days colorless and clear crystals of MgF_2 with a length of up to 10 millimeters had deposited at the less hot zone of the ampoule (sink). Crystals were mechanically removed from the silica tube walls and used for the investigation in the TEM (for more details cf. (32)).

2.2. Specimen Preparation

The MgF_2 crystals were crushed in an agate mortar and dispersed on holey carbon foil on copper grids. Contamination with water was deliberately avoided. The specimen was examined at 300 kV with a Philips CM 30 (side entry goniometer, high-resolution stage) equipped with a PEELS 666 (Gatan) (6, 16, 20) and an EDAX PV 9900 with Si(Li) detector.

3. EELS ANALYSIS OF MgF_2 SAMPLES DURING IRRADIATION IN TEM

3.1. Experimental Conditions

EELS measurements were performed under identical conditions to get comparable results (see Table 1). In a beam, with weak intensity to avoid any damage before the EELS analysis started, a crystal was searched and centered. At this crystal at intervals of 3 minutes, 20 spectra were acquired with an integration time of 8 sec each, one after another (8, 17). At the end of the analysis the interval was increased because there was no significant change in the spectra anymore. During the analysis the crystal was not moved.

After 7 hours there were approximately 400 single spectra received. Each was quantified according to the widely known procedure mentioned in the literature (4, 14, 28).

The analyzed spectra were normalized to the Mg *K* edge because the Mg part was over the time constant (see below).

3.2. Experimental Procedure and Results

At the beginning of an experiment we found Mg and F in the first EEL spectra and only a negligible trace of oxygen. But in the next 3 to 10 minutes of irradiation the amount of F decreased dramatically. It is very remarkable that at the same time the amount of oxygen did not increase in the same way as the amount of fluorine decreased. The O *K* edge grew in intensity as late as about 45 minutes. Figure 2 shows the change of the spectra during the analysis.

The quantification of the first few spectra gave the expected ratio F/Mg ≈ 2/1. Figure 3 shows the ratio F/Mg as well as the ratio O/Mg as a function of time. With arctan functions we achieved the best fit to the values. The fitted functions show the tendencies of the results of the quantifications.

- function for F/Mg:

$$f(t) = \arctan(-227.5\ (t - 271.3)) + 3.1 \qquad [1]$$

- function for O/Mg:

$$f(t) = \arctan(15186.9\ (t - 7188.5)) + 0.7. \qquad [2]$$

As one can see the F/Mg ratio starts at about 2. After ~ 150 sec the ratio decreases rapidly and tends at the end of the decomposition to zero.

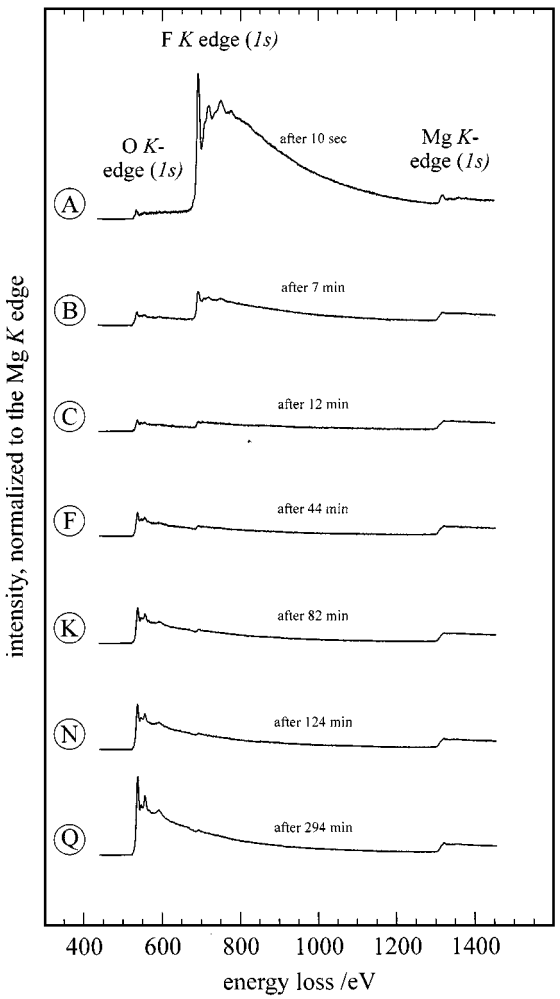

FIG. 2. *K* edges of O, F, and Mg from the MgF_2 sample at different times. The spectra are normalized to the Mg *K* edge and shifted along the intensity axis (dispersion 1 eV/channel).

The ratio O/Mg starts at about 0.08 and stays around 0.1 until $\sim 10^{3.3}$ sec. After that it increases and finally heads towards a ratio of 1.

As in Fig. 2 one can find the same behavior: the loss of fluorine is not simultaneous with the absorption of oxygen. This happens perceptibly after about 45 minutes ($\triangleq 2700$ sec $\triangleq 10^{3.4314}$ sec) of irradiation, at a time when most of the fluorine has already vanished. Every crystal showed a slightly different time dependence, which could be determined for a particular crystal with a given thickness. But the behavior was always the same.

It was possible to normalize the spectra to the Mg *K* edge, because the amount of Mg did not change remarkably during the analysis. It was measured independently by EELS and EDX analysis with an internal standard. As internal standard for EELS the carbon *K* edge was taken, coming from the foil on the grid. In EDX we used the copper peaks coming from the grid as the internal standard. The two standards did not change during the analysis, so the ratios Mg/C and Mg/Cu, respectively, should be over the time the same, if the amount of Mg remains always stable. The constant amount of Mg, which means $\sum \mathrm{Mg} \triangleq (\mathrm{Mg}^{2+} + \mathrm{Mg}^{\pm 0}) = \text{const.}$, was in both cases observed and confirmed.

The irradiation obviously not only leads to the destruction of the crystal lattice, but it comes simultaneously to chemical reactions where MgF_2 is the starting material and MgO is the end product. As the comparison of the electron loss near-edge structures (ELNES) in Figs. 4 and 5 shows, the spectrum of the MgF_2 sample at the end of the decomposition and the spectrum of MgO have nearly the same features. The O *K* edges have the same ELNES (cf. Fig. 5a) and the Mg *K* edges are almost similar, although due to the bad statistic of the Mg *K* edge from the MgF_2 sample the noise is fairly strong in that spectrum (cf. Fig. 5b).

The decomposition of MgF_2 by an electron beam ends with MgO. But which phase is present in the time interval from $\sim 10^{2.2}$ sec to $\sim 10^{3.3}$ sec (cf. Fig. 3)? Neither with EELS nor with EDX could elements other than Mg, F, and O be found and the amount of Mg remained constant over time. Therefore, the conclusion is that elemental magnesium appears as an intermediate during the decomposition.

The results of the EELS analysis suggest that the conversion of MgF_2 proceeds via elemental Mg to MgO. In Fig. 6 a simplified description of the process of conversion is given qualitatively.

The stages of this process should be visible in electron diffraction images, too, because the time window of the

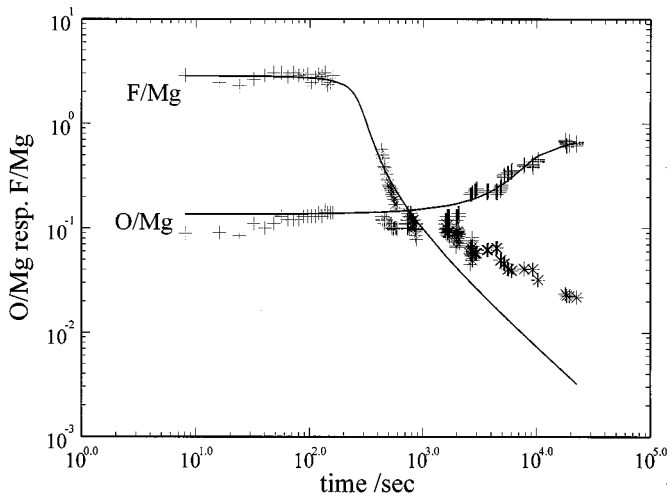

FIG. 3. F/Mg ratio, resp. O/Mg ratio, versus time, results of the quantification from the EEL spectra for F/Mg (∗), resp. O/Mg (+), against the time in seconds (double logarithmical plot). The two solid lines are fitted arctan functions (cf. Eqs. [1] (F/Mg) and [2] (O/Mg)).

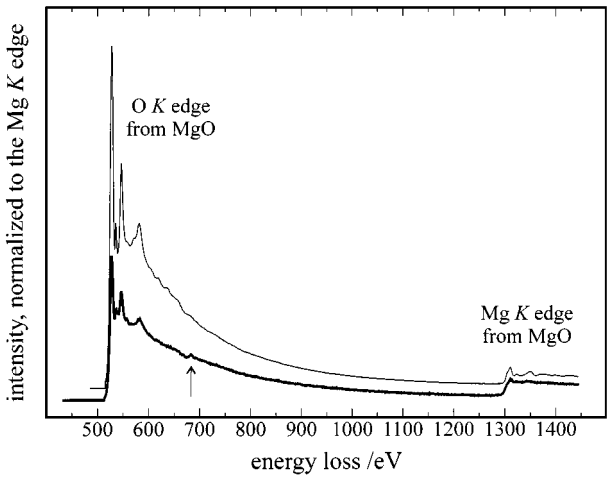

FIG. 4. EEL spectra from MgF_2 at the end of the decomposition (boldfaced), and from MgO. The arrow marks the remaining F *K* edge. The similarity between the two spectra is obvious. The spectra are background substracted, deconvoluted, shifted along the intensity axis, and normalized to the Mg *K* edge (dispersion 1 eV/channel).

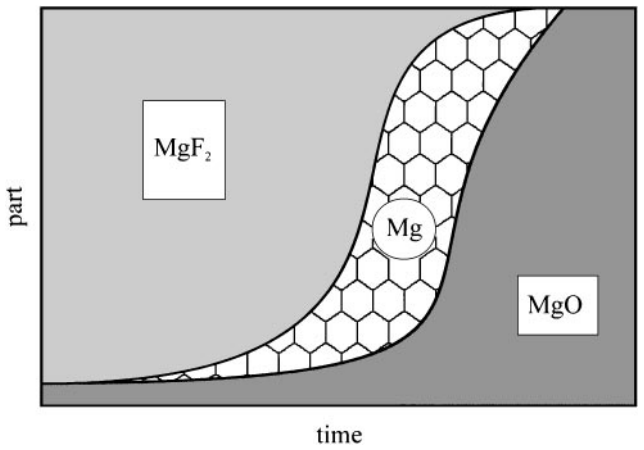

FIG. 6. Progress of the decomposition of MgF_2 caused by electron beam irradiation in the TEM derived from the results of the EELS analysis (simplified). The observed amount of O at the beginning is shown under the assumption that it is present as MgO.

existence of elemental Mg should be large enough to obtain diffraction patterns.

4. DIFFRACTION ANALYSIS OF MgF_2 AND ITS DECOMPOSITION PRODUCTS IN TEM

To check the reliability of the EELS results the products of the decomposition of MgF_2 were investigated apart from EELS with the method of electron diffraction in the TEM. Independent from EELS, electron diffraction was applied to the decomposition process of MgF_2. The aim was to prove the appearance and fading of the phases MgF_2 and elemental Mg as well as MgO by electron diffraction during the irradiation experiment.

4.1. Experimental Procedure

A suitable crystal, once found, was adjusted into the desired orientation (goniometer stage). This was performed with as little electron irradiation as possible to avoid decomposition at that stage. Using the selected area electron diffraction (SAED) aperture the area of the sample was selected. After the diffraction pattern of the starting phase

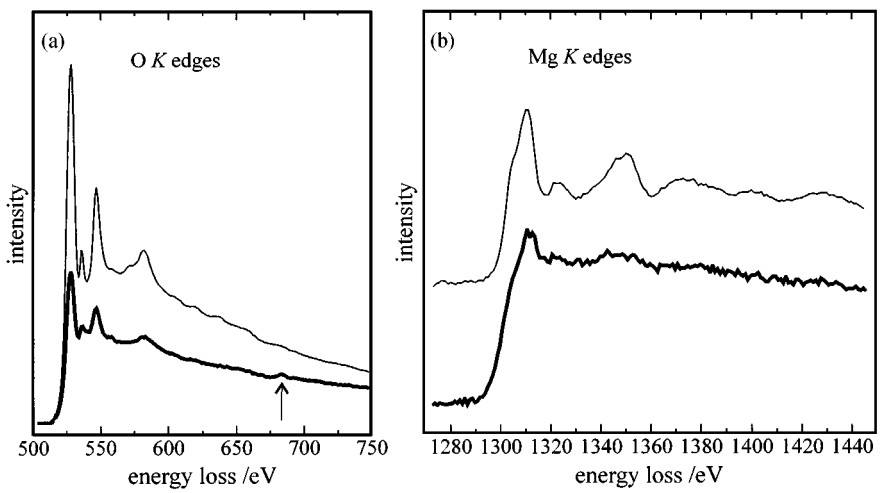

FIG. 5. O *K* edge (a) and Mg *K* edge (b) from MgO, resp. from a MgF_2 sample (boldfaced), at the end of the decomposition. The arrow marks the remaining F *K* edge. The similarity between the two spectra in (a) as well as in (b) is obvious. The spectra are background substracted, deconvoluted, and normalized to the Mg *K* edge (dispersion 1 eV/channel). In spectrum (b) the Mg *K* edge of MgO is shifted along the intensity axis.

TABLE 2
Crystal Data for MgF_2, Mg, and MgO Used for the Calculation of *d* Values

		Space group	Lattice constants
MgF_2	Tetragonal, rutile type (27)	$P4_2/mnm$ (No. 136)	$a = b = 4.6181$ Å $c = 3.0463$ Å $\alpha = \beta = \gamma = 90^\circ$
Mg	Hexagonal, hcp (29)	$P6_3/mmc$ (No. 194)	$a = b = 3.2093$ Å $c = 5.2103$ Å $\alpha = \gamma = 90^\circ$ $\beta = 120^\circ$
MgO	Cubic, halite type (23)	$Fm\bar{3}m$ (No. 225)	$a = b = c = 4.2171$ Å $\alpha = \beta = \gamma = 90^\circ$

MgF_2 was adjusted (along c^*), the specimen was not moved for the rest of the experiment. The irradiation of the specimen was performed under the same conditions as in the EELS analysis (cf. Section 3). Many crystals had to be examined to get satisfying diffraction patterns, because in some cases the decomposition happened too fast to be recorded.

Table 2 gives the crystal data of the three phases, which we are interested in. They are well known and from the diffraction patterns it is possible to calculate the *d* spaces:

$$d = \frac{\lambda L V_{\text{sec}}}{r}, \qquad [3]$$

with

d = *d* space (Å),
λ = wavelength of the electrons (Å), 0.0197 Å,
L = camera length (mm),
V_{sec} = magnification by photography ($V_{\text{sec}} = V_{\text{prim}} x$, with x = magnification factor)
r = distance between primary beam and diffraction spot, ring, respectively (mm).

The observed *d* spaces were compared with those calculated from the crystal data (cf. Table 2; *d* space calculation cf. e.g. (10); for the compared *d* spaces see Tables 3 and 4).

TABLE 3
Comparison between the Observed and Calculated (29) d_{101} Values from a Powder Electron Diffraction Pattern from Mg

	Observed	Calculated
d_{101}/Å	1.90	1.838

TABLE 4
Comparison between the Observed and Calculated (23) d_{hkl} Values from a Powder Electron Diffraction Pattern from MgO

	Observed	Calculated
d_{111}/Å	2.57	2.4348
d_{002}/Å	2.23	2.1086
d_{202}/Å	1.60	1.4910
d_{222}/Å	1.28	1.2174

4.2. Results

Figure 7 shows the brightfield image of a MgF_2 crystal before decomposition could be detected. The accompanying electron diffraction pattern shows the spots of the typical tetragonal rutile structure. The two a* axes can be seen. The interpretation of those diffraction images gave the lattice constants of MgF_2 (here $a = b$). The primary beam stopper indicates the area which was used for the diffraction.

At the beginning of the decomposition process the diffraction pattern of MgF_2 disappeared in the irradiated area after 1.5 to 5 minutes. Instead of the spots, diffraction rings appear, typical for electron diffraction on powders. After about 3.5 minutes the powder pattern in Fig. 8 was recorded. It shows reflections which are concentrically arranged. The strongest ring corresponds to the 1 0 1 ring of the simulation of Mg diffraction patterns. The inserted

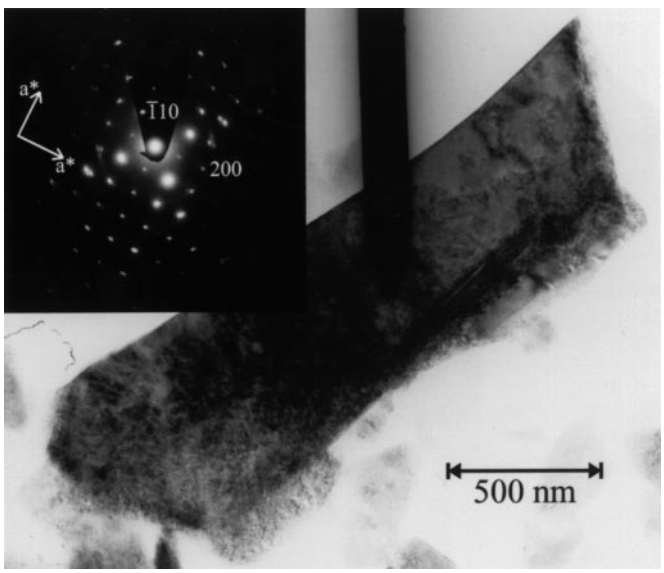

FIG. 7. Brightfield image of a MgF_2 crystal with the corresponding electron diffraction pattern, direction along c^*, camera length $L = 300$ mm, scale in figure.

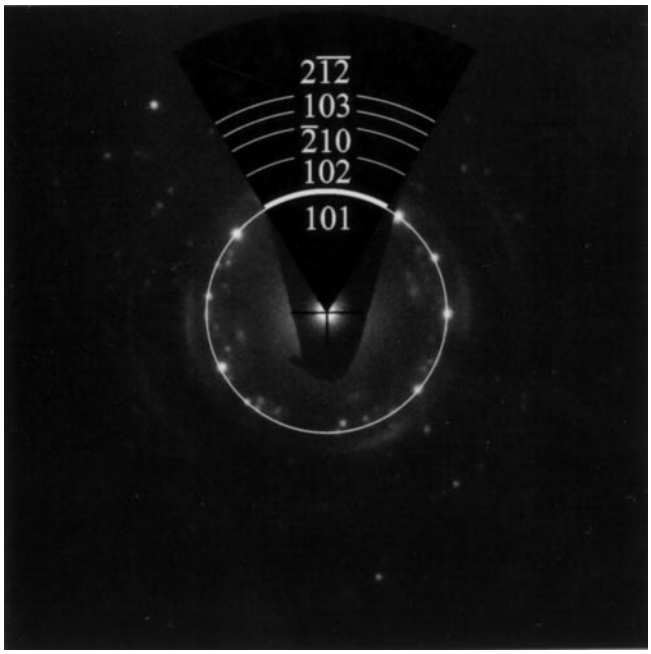

FIG. 8. Electron diffraction of a damaged specimen area of MgF_2 crystal after 3.5 minutes of irradiation. The inserted simulation of the powder pattern of Mg shows the rings to be expected (25). The line thickness of the simulated pattern correlates directly to the intensity of the rings. In the obtained pattern the 1 0 1 ring from Mg can be identified, the circle of the simulation connects the weak reflections. All other rings cannot be seen because of their very poor intensity (cf. the simulation).

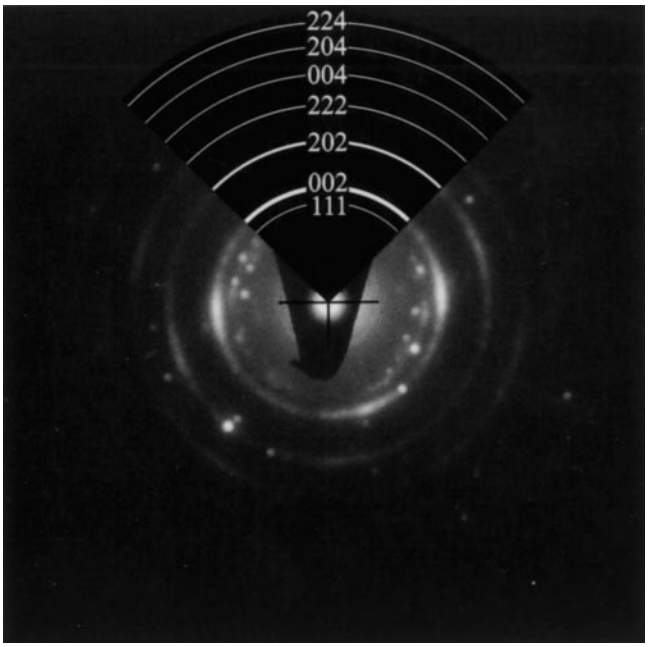

FIG. 9. Electron diffraction of the same damaged specimen area of a MgF_2 crystal as in Fig. 8 after 45 minutes of irradiation. The diffraction rings can definitely be related to the simulation (25). The line thickness of the simulated pattern correlates directly to the intensity of the rings.

simulation of the powder pattern of Mg shows the expected rings (25) and the line thickness of the simulated pattern correlates directly with the intensity relation of the rings. In the simulated pattern of Mg the 1 0 1 ring is the strongest ring; it can be recognized in the obtained diffraction pattern. The observed and calculated d values of the 1 0 1 ring correspond reasonably well (Table 3). All other rings could not really be seen because of their very poor intensity.

The circle formed by the concentric spots in Fig. 8 cannot come from MgO (e. g. 1 1 1), because the other more intense rings should be visible as well. This was not observed. During a further period of irradiation the diffraction rings of Mg faded away but a new pattern appeared instead. This was the diffraction pattern of MgO as can be seen in Fig. 9. Figure 9 was recorded after 45 minutes. The inserted simulation (25) shows that the four inner circles certainly came from MgO after 45 minutes. Again, the line thickness of the simulated pattern correlates directly with the intensity of the rings.

The powder diffraction pattern from the indicated area at the crystal after 6.5 h of irradiation is shown in Fig. 10 . This is definitely a pattern from MgO. Even the intensity differences can be observed as in the simulation. The observed and calculated (from lattice constants (23)) d values are in good correspondence (cf. Table 4).

After a long time of irradiation there is microcrystalline MgO at the damaged area of the specimen. In Fig. 10 the

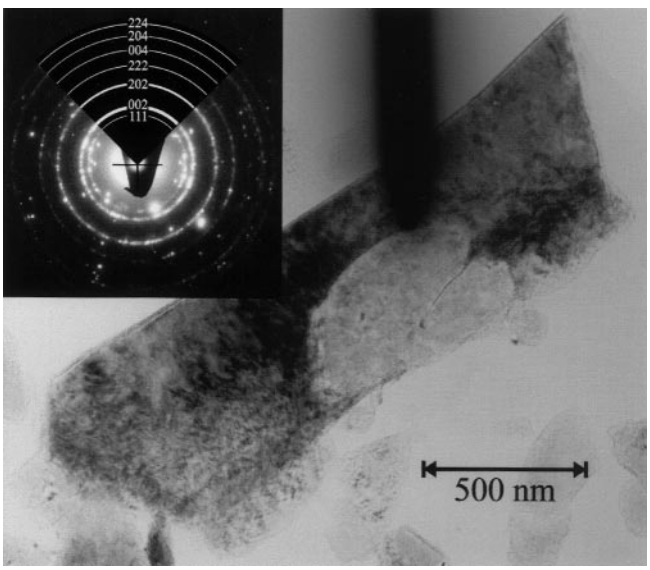

FIG. 10. Brightfield image of a MgF_2 crystal after 6.5 h. The diffraction pattern was made from the area to which the primary beam stopper points; the inserted simulation gives the expected powder pattern of MgO, which fits very well on the observed powder pattern of the semicircle of the damaged area.

primary beam stopper points at an area where the decomposition has far proceeded. It is recognizable as a brighter semicircle within the still intact crystalline MgF_2.

The *powder* pattern of MgF_2 was never observed with SAED in the experiments described.

5. DISCUSSION

The EELS analysis as well as the diffraction investigations gave evidence that in the electron beam the decomposition of MgF_2 passes over elemental Mg metal to the microcrystaline end product MgO. The process can be described in two equations which proceed one after another:

$$MgF_2 \rightarrow Mg + F_2\uparrow \quad \text{and} \qquad [4]$$

$$Mg + \tfrac{1}{2}O_2 \rightarrow MgO. \qquad [5]$$

In (7) the decomposition of CaF_2 and SrF_2 caused by electron beam irradiation led to the elemental metal as could be proven by the respective Moiré pattern. But those patterns vanished after a short time of further irradiation. The author gave no further explanation for it.

From the results of this work we are able to conclude the analogy to the case of MgF_2: in all probability the decomposition of CaF_2/SrF_2 leads over the metal to the microcrystaline oxide, which could not be recognized by Moiré patterns.

It was very difficult to obtain diffraction images because the structures were very sensitive to the stress caused by irradiation. The decomposition took place so quickly that it was difficult to take a photograph. Nevertheless, we were still successful. In some cases we observed that the decomposition area spread concentrically. In high-resolution mode this behavior was even faster. Every attempt to obtain high-resolution images of the irradiated area failed immediately because of the rapid decomposition of the specimen.

The decomposition seems to be stronger in compounds with a high ionic part of the bonding (13). The reason could be a partial heating of the specimen area, which is hard to measure experimentally. The heating of the specimen is produced by phonon excitation. That means also that the heating can be reduced other than by cooling by a high accelareting voltage and thin specimens, because the mean free path of phonon excitation is relatively large.

Under the conditions we used ($U = 300$ kV, thin specimens) phonon excitation is probably not the main cause for the decomposition of MgF_2 by the electron beam.

The excitation of the electrons between different bands (ionization processes) can be compensated not only by the generating of Auger electrons and photons but also in a special mechanism by excitons. This is probably the reason for the decomposition of MgF_2.

Question of the mechanism of the decomposition now presents itself.

It is presumed that no fluoride or fluorine is directly struck from the crystal lattice because of its many times higher mass compared to that of an electron.[3] More probable is the interaction between the beam electrons and the (binding) electrons of the compound—an ionization.

In this case a redox reaction is initiated by the beam. In this reaction F^- may be oxidized and may leave the specimen as volatile F_2 (cf. Fig. 11a).

The remaining electrons form F centers (color centers (cf. (19)), Fig. 11b); those reduce Mg^{2+} to Mg metal, which is finally oxidized by oxygen to MgO.

One can regard the three different structures each as a hexagonal arrangement, although this arrangement in MgF_2 is distorted (cf. Figs. 11a to 11c). The distance from one Mg atom to the next closest is in all three structures around 3 Å as shown in Fig. 11. Corresponding to the Mg atoms there is obviously not such a big change from one structure to the other in all three cases.

Independently recorded EEL spectra from MgO showed the same appearance as those obtained after the decomposition of MgF_2 (cf. Figs. 4, 5, and 12).

The examination of the ELNES (21), which is not explained closely in the text above, gave also important hints about the proceedings during the decomposition of MgF_2. Not only the EELS and the diffraction analysis conclude the unusual result of the formation of Mg metal but also the comparison of the near-edge structure (ELNES) of the Mg *K* edge at different times of the decomposition of the same specimen area. Before any decomposition was observed one can see the Mg *K* edge with a very distinctive ELNES in MgF_2 (see Fig. 12, after 10 sec). This ELNES is lost during further irradiation while Mg metal is produced (see Fig. 12 after 12 min). This edge reminds us of edges of elemental metals like copper $Cu^{\pm 0}$. $Cu^{\pm 0}$ has an edge structure similar to that of Mg. In CuO the copper edge shows a very distinct ELNES (18, 31) as well as the Mg edge in MgO.

At the end of the decomposition one can observe the development of a new ELNES in the Mg *K* edge. This is a typical ELNES for Mg^{2+} in an octahedral environment, as Mg is octahedrally surrounded by oxygen in MgO (e. g. (22), cf. the Mg *K* edge coming from MgF_2 after 10 sec with the respective Mg *K* edge from MgO in Fig. 12).

Where does the oxygen come from?

The specimen was located in the TEM in an evacuated chamber where the pressure should be no higher than $\sim 10^{-5}$ Pa. The used TEM (CM 30, Philips) reaches this value easily; the rest gas probably does not supply the oxygen. A reaction as in Eq. [6]

$$MgF_2 + H_2O \rightarrow MgO + 2HF, \qquad [6]$$

is rather unlikely with respect to the appearance of metallic magnesium.

[3] But there were cases where W atoms (sic) had been struck by highly accelerated electrons ($U = 1000$ kV) out of a crystal lattice (11).

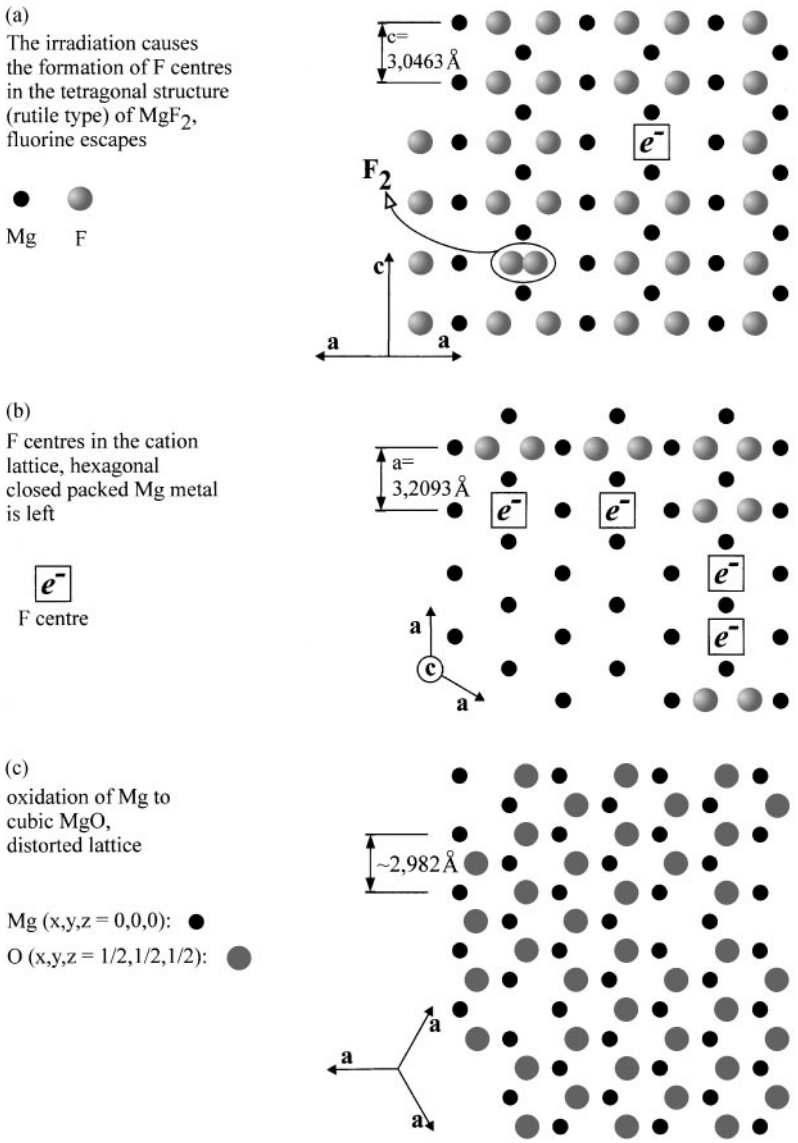

FIG. 11. Proposition of the decomposition mechanism of MgF_2 under electron irradiation in the TEM. (a) and (b) in the figure shows only one plane in a two-dimensional projection; (c) shows two planes.

Oxidation at the end of the decomposition process of Mg, described as

$$Mg + H_2O \rightarrow MgO + H_2\uparrow, \qquad [7]$$

is even more probable than the direct oxidation by O_2 because of the relatively higher amount of water in the vacuum system.

Figure 13 gives an indication of the origin of oxygen.

At the beginning the observed O *K* edge (Fig. 13, after 20 sec) shows a different ELNES than after 25 minutes. Peak a is missing at the beginning of any decomposition and appears in the O *K* edge of MgO for the first time (cf. also Figs. 4 and 5a). Peak a′ can be seen in every spectrum, but becomes distinctive first in the second spectrum.

This indicates that the oxygen which can be seen at the beginning is not in the same chemical environment as the latter in MgO.

This means for the origin of oxygen that it adhears to the specimen and comes into the specimen chamber with the specimen holder, the grid, and specimen. The changes in the spectrum over time exclude the possibility that the MgF_2 crystals are covered with MgO on the surface. Oxygen is probably brought into the system in the form of water and/or O_2.

Whether the change of the F *K* edge (Fig. 13), especially in peaks b and b′, results from the oxidation $2F^- \rightarrow F_2 + 2e^-$ could not be decided finally. The change in the ELNES is remarkable. It shows a new chemical environment for

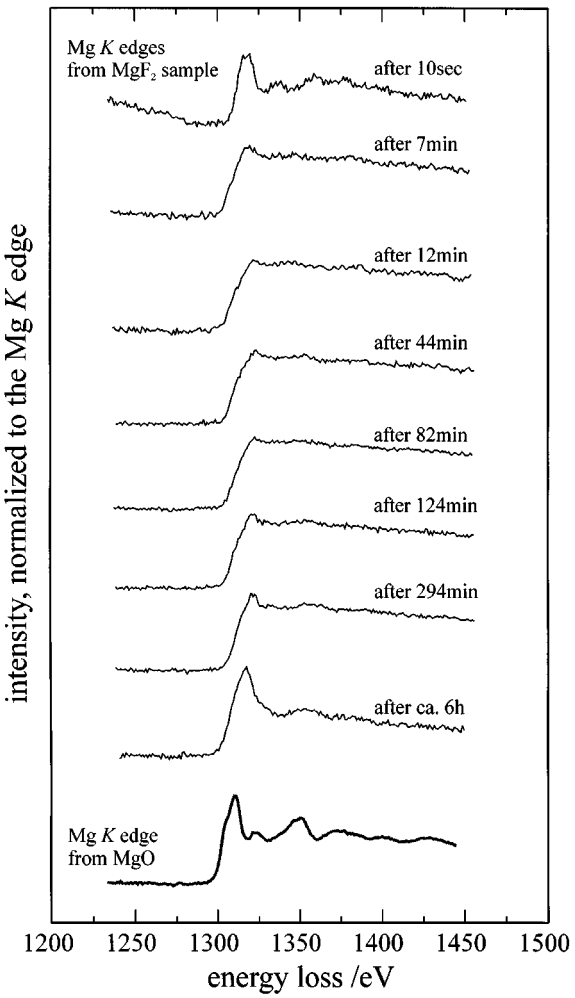

FIG. 12. Change of the Mg *K* edge during the decomposition of MgF_2 in the TEM. The spectra are background corrected, deconvoluted, and shifted along the intensity axis (dispersion 1.0 eV/channel, detail). Below (boldfaced) is given the spectrum from MgO.

flourine compared to MgF_2 and appears as a new peak (see arrow in Fig. 13).

It is remarkable that we did not find the decomposition of MnF_2 under the same conditions as for MgF_2.

In the future the decomposition of MgF_2 in the electron beam would be a very interesting subject for real-time TV images. Model calculations for this system seem to be promissing, too, as they are reported for the decomposition of alkaline earth carbonates (2) and for the respective peroxides (3).

ACKNOWLEDGMENT

Thanks are due to the Deutsche Forschungsgemeinschaft for the support of this work.

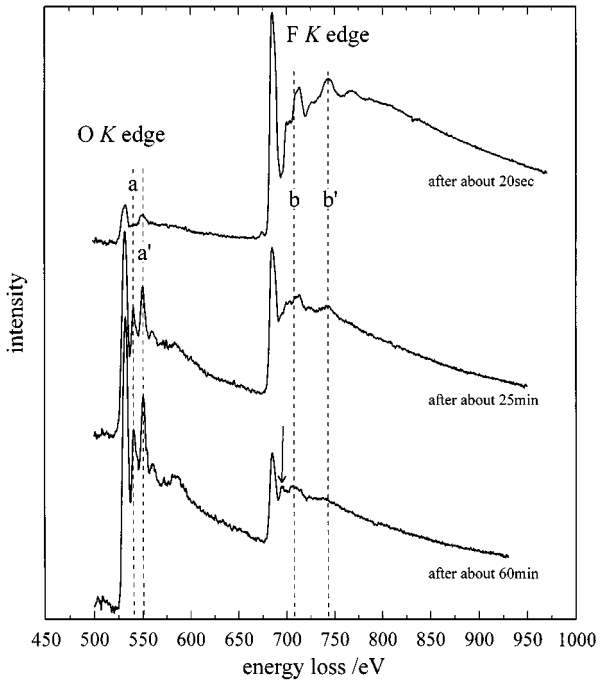

FIG. 13. Change of the *K* edges of O and F during the decomposition of MgF_2 in the TEM. The spectra are background corrected, deconvoluted, and shifted along the intensity axis (dispersion 0.5 eV/channel); for further explanations see the text.

REFERENCES

1. E. D. Cater and P. R. Buseck, *Ultramicroscopy* **18,** 241–252 (1985).
2. A. de La Croix, R. B. English, M. E. Brown, and L. Glasser, *J. Solid State Chem.* **137,** 332–345 (1998).
3. A. de La Croix, R. B. English, M. E. Brown, and L. Glasser, *J. Solid State Chem.* **137,** 346–352 (1998).
4. R. F. Egerton, "Electron Energy-Loss Spectroscopy in the Electron Microscope," 2nd Ed. Plenum Press, New York, 1996.
5. R. F. Egerton, P. A. Crozier, and P. Rice, *Ultramicroscopy* **23,** 305–312 (1987).
6. R. F. Egerton, Y.-Y. Yang, and S. C. Cheng, *Ultramicroscopy* **48,** 239–250 (1993).
7. T. Evans, *Philos. Mag.* **8,** 1235–1240 (1963).
8. "Modell 666, Parallel Detection Electron Spectrometer—Instruction Manual," Gatan, 1988.
9. R. Gruehn and R. Glaum, *Angew. Chem., Int. Ed.* **39,** 692–716 (2000).
10. "International Tables of Crystallography" T. Hahn and D. Riedel, Vol. A, 3rd Ed. Kluwer Academic, Dordrecht, 1993.
11. S. Horiuchi, *Chem. Scr.* **14,** 75–81 (1978/79).
12. D. G. Howitt, *in* "Principles of analytical electron microscopy" (D. C. Joy, A. D. Romig, and J. Goldstein, Eds.), pp. 375–392. Plenum, New York, 1986.
13. J. J. Hren, *in* "Principles of analytical electron microscopy" (D. C. Joy, A. D. Romig, and J. Goldstein, Eds.), pp. 353–374. Plenum, New York, 1986.
14. D. C. Joy, *in* "Principles of analytical electron microscopy" (D. C. Joy, A. D. Romig, and J. Goldstein, Eds.), pp. 249–276. Plenum, New York, 1986.
15. M. N. Kabler and R. T. Williams, *Phys. Rev. B* **18,** 1948–1960 (1978).

16. O. L. Krivanek, C. C. Ahn, and R. B. Keeney, *Ultramicroscopy* **22,** 103–116 (1987).
17. M. K. Kundman and O. L. Krivanek, *Microsc. Microanal. Microstruct.* **2,** 245–256 (1991).
18. R. D. Leapman, L. A. Grunes, and P. L. Fejes, *Phys. Rev. B* **26,** 614–635 (1982).
19. L. E. Murr, *Phys. Stat. Sol. A* **22,** 239–251 (1974).
20. M. Nelhiebel, M. Schenner, and P. Schattschneider, *Ultramicroscopy* **65,** 199–203 (1996).
21. P. Rez, X. Weng, and H. Ma, *Microsc. Microanal. Microstruct.* **2,** 143–151 (1991).
22. M. Sanchez del Rio, J. Garcia, R. Gonzalez, M. Benfatto, and A. Bianconi, *Physica B* **158,** 527–528 (1989).
23. S. Sasaki, K. Fujino, and Y. Takeuchi, *Proc. Jpn. Acad.* **55,** 43–48 (1979).
24. H. Schäfer, "Chemical transport reactions." Academic Press, New York, 1964.
25. P. A. Stadelmann, *Ultramicroscopy* **21,** 131–146 (1987).
26. J. Strane, L. D. Marks, D. E. Luzzi, M. I. Buckett, J. P. Zhang, and B. W. Wessels, *Ultramicroscopy* **25,** 253–258 (1988).
27. G. Vidal-Vadat, J. P. Vidal, C. M. E. Zeyen, and K. Kurki-Suonio, *Acta Crystallogr. B* **35,** 1584–1590 (1979).
28. D. B. Williams, "Practical Analytical Electron Microscopy in Material Science." VCH, Weinheim, 1984.
29. R. W. G. Wyckoff, "Crystal Structures," 2nd Ed. Wiley, New York, 1965.
30. Y. Yokota, H. Hashimoto, and T. Yamaguchi, *Ultramicroscopy* **54,** 207–214 (1994).
31. L.-P. Zenser, Dissertation, Universität Giessen, 1999.
32. L.-P. Zenser, R. Gruehn, and M. Weil, *Z. Anorg. Allg. Chem.* **626,** 871–877 (2000).